Nano-Structured Bio-Inorganic Hybrid Material for High Performing Oxygen Reduction Catalyst

Rongzhong Jiang,* Dat T. Tran, Joshua P. McClure, and Deryn Chu

Sensors and Electron Devices Directorate, U.S. Army Research Laboratory, 2800 Powder Mill Road, Adelphi, Maryland 20783-1197, United States

S *Supporting Information*

ABSTRACT: In this study, we demonstrate a non-Pt nanostructured bioinorganic hybrid (BIH) catalyst for catalytic oxygen reduction in alkaline media. This catalyst was synthesized through biomaterial hemin, nano-structured Ag−Co alloy, and graphene nano platelets (GNP) by heat-treatment and ultrasonically processing. This hybrid catalyst has the advantages of the combined features of these bio and inorganic materials. A 10-fold improvement in catalytic activity (at 0.8 V vs RHE) is achieved in comparison of pure Ag nanoparticles (20−40 nm). The hybrid catalyst reaches 80% activity (at 0.8 V vs RHE) of the state-of-the-art catalyst (containing 40% Pt and 60% active carbon). Comparable catalytic stability for the hybrid catalyst with the Pt catalyst is observed by chronoamperometric experiment. The hybrid catalyst catalyzes 4-electron oxygen reduction to produce water with fast kinetic rate. The rate constant obtained from the hybrid catalyst (at 0.6 V vs RHE) is 4 times higher than that of pure Ag/GNP catalyst. A catalytic model is proposed to explain the oxygen reduction reaction at the BIH catalyst.

KEYWORDS: bio-inorganic hybrid catalyst, oxygen reduction reaction, Ag−Co, hemin, graphene nanoplatelets
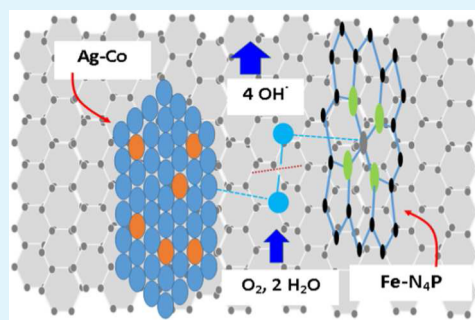
1. INTRODUCTION

Fuel cells have demonstrated promise for providing clean electric power to automobiles, unmanned aerial vehicles (UAVs), submarines, and consumer electronics. However, commercialization of fuel cells is challenging due to the high cost of materials, low performance, and fast degradation of various fuel cell components. In particular, the electrocatalyst is one of the most important components in a fuel cell and plays a vital role in the fuel oxidation and oxygen reduction reactions. The catalysts' performance directly affects the power efficiency, energy density, and operational lifetime of a fuel cell. The state-of-the-art catalysts for fuel cells are expensive noble metals (e.g., platinum black and platinum-based metal alloys). For a polymer electrolyte membrane fuel cell (PEMFC) designed for automotive applications, the catalyst accounts for approximately 60% of the total cost of a fuel cell.[1] Therefore, the development of low cost, highly active, and stable catalyst materials is warranted, and many researchers have taken various approaches to solve the challenge. For example, Anson and Collman et al. have synthesized and tested organic dimeric cofacial cobalt porphyrins that catalyze dioxygen via a 4-electron pathway to produce water.[2,3] Despite best efforts, the catalytic activity of most organometallic macrocycles prove to be not stable in acidic electrolytes. In the past several years, heat-treatment approaches[4−7] have been adopted to enhance the stability of these transition metal macrocycles. Although the performance of these catalysts is much improved after heat-treatment, it does not meet or exceed practical requirements when compared to the performance of platinum (i.e., electrocatalytic activity and

stability). Improvements in catalytic activity have been realized through the emergence of nanotechnology-related material synthesis and processing designs,[8] such as, bucky paper,[9] carbon nanotube,[10,11] nanofiber,[12] mesoporous carbon,[13] and graphene.[14] These nano materials can either be used as catalyst supports or directly as a catalyst. In recent years, a lot of nanostructured noble metals and alloys, such as metal nanoparticles,[15] nanowires,[16] nanoframes,[17−19] nanohol-lows,[20,21] and nanocoreshells,[16,22] have been successfully synthesized and tested for fuel cell catalysts. Although these nanostructured metals have displayed better catalytic activity, the complex synthesis and high cost in materials are not satisfactory for practical applications. In addition to nano-processing, mimicking biologic functions in the synthesis of new functional materials has generated enormous interests. For example, low-cost biomaterials have been utilized for preparation of catalysts, such as enzymes, hemin, hemoglobin, and egg-white protein.[23−27] As is well-known, hemoglobin is an efficient transporter of oxygen in the body, whereby the active part is heme-B, or a form of hemin. The hemin molecule and the iron porphyrin molecule have the same inner porphyrin ring that contains a functional group (Fe−N$_4$P). The functional group grants catalytic activity. Their only difference is the chemical groups linked to the outer porphyrin ring. We utilize nature's catalytic mechanisms by incorporating an active

inorganic material into a catalytic active biomaterial. The hemin is naturally available from animal blood in large quantity, which has much lower cost than using porphyrins that are synthesized artificially. The present research focuses on the synthesis of a nanostructured bioinorganic hybrid (BIH) catalyst with precisely controlled size, shape, and architecture, which is subsequently used to perform the oxygen reduction reaction (ORR). Silver has been well-studied for use as an oxygen reduction electrocatalyst in alkaline media.[28,29] One of the main reasons for the use of silver is that the cost is ~1% of the cost of Pt, and the abundance of silver is approximately 1500% of the abundance of Pt. Moreover, alloying Ag with transition metals, such as Co, results in better catalytic activity.[30] Research on Ag−Co catalyst for oxygen reduction has been reported in 2006 by Lima et al.[30] A few years later, it was reported again by Holewinski et al.[31] However, their results are very different. Lima et al.[30] used both the rotating ring disk electrode method and the Koutecky−Levich method to study oxygen reduction at Ag−Co catalyst. They concluded that oxygen is reduced at Ag−Co catalyst via mix-pathways by 4-electron reaction, and by 2-electron reactions. Holewinski et al.,[31] also studied oxygen reduction at Ag−Co catalyst using Koutecky−Levich method alone. They concluded that oxygen was reduced at Ag−Co catalyst mainly by 4-electron reaction. We are interested in why they obtained very different results. Therefore, we examined their different synthetic methods for making Ag−Co catalyst. Lima et al. used a water-based solution to synthesize the Ag−Co catalyst at low temperature (60 °C) and used NaBH$_4$ as the reducing reagent. But Holewinski et al.[31] used waterless dry method to synthesize Ag−Co catalyst at a high temperature (500 °C) and used hydrogen gas as the reducing reagent. In this study, we avoided large crystal growth by synthesizing Ag−Co nanoparticles at low temperature. First, we synthesize nanostructured Ag−Co according to the methods reported for making metal nanoframes and nanohollows,[17−21] and interestingly create Ag−Co nanodendrimers. The dendritic nanoparticles showed much higher activity than pure Ag nano particles. Further improvement of the catalytic activity is achieved by incorporating the inorganic Ag−Co into a bioactive material, which is believed to be caused by a synergistic effect between components.[32] Specially, hemin was the bio material, and graphene nano platelets (GNP) was the catalyst support. The hemin and GNP are first uniformly mixed and heat-treated to enhance the activity and stability. Incorporation of Ag−Co nanodendrimers into the heat-treated material of hemin-graphene is achieved by ultrasonically processing. The final product is a BIH catalyst, which is utterly different from those of inorganic Ag−Co catalysts reported by Lima and Holewinski et al.,[30,31] in the catalyst composition, structure, synthesis, function, and design method. To date, there have been no reports on the synthesis of nanostructured BIH catalyst with low-cost bioactive hemin, inorganic Ag−Co dendrimers, and nanosized graphene. The ORR performance of the created BIH catalyst are examined electrochemically in alkaline media.

2. EXPERIMENTAL SECTION

2.1. Chemicals and Materials. Graphene nanoplatelets (GNP) with a BET surface area between 600−650 m^2/g were purchased from Cheap Tubes, Inc. Hemin from porcine, silver nitrate (AgNO$_3$), cobalt(II) oxalate dihydrate (CoC$_2$O$_4$·2H$_2$O), sodium borohydride (NaBH$_4$), and ammonium hydroxide 28% NH$_3$ were purchased from Aldrich. Two baseline catalysts were obtained from Johnson Matthey, including 40% Pt nano catalyst supported on 60% active carbon (40%

Pt/C) and pure Ag-nanopowder (pure Ag-nano, particle size 20−40 nm). Deionized water was used for all synthesis and experiments.

2.2. Synthesis of HT-Hem/GNP. Synthesis of HT-hemin supported on GNP have been reported.[24,25,33,34] The hemin has an inner porphyrin ring (Fe−N$_4$P), located in the center of the molecular. Here, we briefly describe the synthesis. Hemin was uniformly dispersed on GNP by mixing 1.0 g hemin and 1.0 g GNP together with 50 mL N,N-dimethylformamide (DMF). After dried on a hot-plate, the mixture was placed in a ceramic boat and sent to a tubular furnace for heat-treatment by 2−3 h under nitrogen atmosphere at 600 °C, which is the best pyrolysis temperature (400−900 °C) to achieve the optimum catalytic performance. The material after heat-treatment was further ultrasonically processed to finer particles. Ultrasonic treatment was carried out by immersing the targeting material in ice water. The ultrasound generator was a Branson Sonifier 450 Analog Ultrasonic Homogenizer. The material of hemin and GNP after these treatments was dried at 80 °C and named as HT-Hem/GNP (or material A; Figure 1).
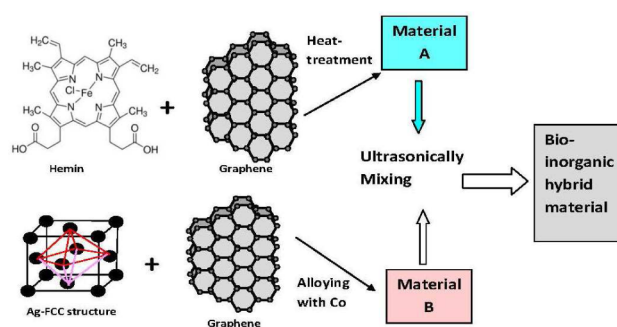
Figure 1. Schematic drawing for synthesis of nanostructured BIH material for high performing oxygen reduction catalyst.

2.3. Synthesis of Ag, Ag−Co and Ag−Co/GNP. Silver ammonia complex was formed by adding 0.83g AgNO$_3$ and 5 mL ammonia hydroxide, and moved into a 250 mL flask containing 80 mL water. Alternatively, different quantity of CoC$_2$O$_4$·2H$_2$O was suspended in 40 mL of water and 5 mL of ammonia hydroxide and moved into the same flask. The reducing reagent was NaBH$_4$ solution by dissolving 0.5 g of NaBH$_4$ in 40 of mL water. The Ag−Co was synthesized by slowly dropping the NaBH$_4$ solution into the flask and fast stirring. Nitrogen gas was used to cover the surface of the reaction solution in the flask. Dark precipitate was formed with adding NaBH$_4$ solution. The precipitate was separated by centrifugation and washed with water eight times and with acetone one time, respectively. The product was dried at 80 °C. The amount of Co in the Ag−Co alloy was controlled by adjusting the Co/Ag ratio in the synthesis. The Ag content in the Ag−Co alloy was determined by gravimetrical analysis, in which hydrochloric acid was used to thoroughly remove the Co element in the Ag−Co alloy, and weighing the dry Ag powder. Three samples of Ag−Co alloys were obtained with Co/Ag atomic ratio in 0.05, 0.10 and 0.20, respectively. The pure Ag fine power was synthesized with the same method of making Ag−Co but without adding cobalt oxalate in the reaction solution. The Ag−Co/GNP (material B; Figure 1) was synthesized with the same method of making Ag−Co with 0.10 Co/Ag atomic ratio, except a quantitative amount of GNP was added in the reaction solution before dropping NaBH$_4$ solution in the flask. The sample of Ag−Co/GNP synthesized contains 30% Ag−Co alloy and 70% GNP. The overall content of Ag−Co/GNP contains 28.5% Ag, 1.5% Co, and 70% GNP in mass ratio.

2.4. Synthesis of BIH Catalyst. The nanostructured BIH catalyst was synthesized by ultrasonically processing material A and material B. Figure 1 shows a schematic drawing for synthesis of BIH catalyst for high performing oxygen reduction catalyst. The GNP in the hybrid material is used to promote catalytic site distribution more uniformly. Because the nanoparticles of the two materials are nanoscaled mixed and optimally contacted, the electron transfer between the catalytic

sites will be improved. In addition, because there are two types of catalytic sites (Ag in the Ag−Co alloy and Fe−N$_4$P in the HT-Hemin) provided by two different materials, a synergic effect is expected, which will further improves the catalytic performance. Here, 41 mg Ag−Co/GNP (material B) and 41 mg HT-Hem/GNP (material A) were added into a solution containing 3 mL of water and 3 mL of 1-propanol to form a suspension. This suspension was cooled with ice and ultrasonically treated for 30 min with a Branson Sonifier 450 at duty cycle 40 and output control 8. The dried material after ultrasonic treatment is called as BIH catalyst. The BIH catalyst synthesized in this procedure contains 14.2% Ag, 0.8% Co, 25.0% Hemin, and 60% GNP in mass ratio. The overall synthesis is simple and is easy to scale up to manufacturing production. Although the BIH catalyst contains Ag−Co, it is only one of the components used for synthesis of the BIH catalyst.

2.5. Instrumental Analysis. Transmission electron microscopy (TEM) and scanning transmission electron microscopy (STEM) were obtained with a high-resolution JEOL 2100 FE instrument equipped with an EDAX X-ray detector and a high-angle annular dark field (HAADF) detector. Before imaging, a solution was prepared by adding 5 mg of the catalyst into 5 mL of 1-propanol followed by a short ultrasonic bath (Branson 3510) treatment. An aliquot of ink was loaded onto a C-flat Holey Carbon Grid (1.2 μm hole, 1.3 μm space, 200 mesh, Electron Microscopy Science) with a micropipette, and the sample was dried overnight at room temperature. Selected area electron diffraction (SAED) and energy-dispersive X-ray spectroscopy (EDS) were obtained during the measurements. Scanning electron microscopy (SEM) was obtained with FEI QUANTA 200F instrument. The sample for SEM imaging was prepared by directly loading a small amount of catalyst powder on a sample holder. X-ray diffraction (XRD) was conducted with a Rigaku Ultima III instrument with Cu Kα radiation (λ = 1.5418 Å) using a Bragg−Brentano configuration. The measurements were conducted with scan rate of 1.0° (2θ) per minute; and each diffraction data point was collected at the interval of 0.02 degree (2θ) for the total spectrum range of 10−90° (2θ).

2.6. Electrochemical Characterization. A Pine Bipotentiostat RDE4 was used for electrochemically evaluating the catalysts by depositing the catalyst ink onto a glassy carbon (GC) disk electrode. A catalyst sample was first suspended in 1:1 water/1-propanol solution with a small bottle and cooled with ice. The catalyst ink was prepared by ultrasonic treatment with a Branson Sonifier 450 at a duty cycle 40 and output control 8 for 10 min. The final content of Ag, Ag−Co, or BIH catalyst ink was 4 mg/mL after excluding the mass of GNP. Next, 5 μL of catalyst ink was coated on a GC disk working electrode (0.196 cm^2) and dried at 40 °C for ~60 min. The final coating on the GC disk electrode contained 95% total catalyst and 5% dry Nafion with a Ag or Ag−Co loading of 0.1 mg/cm^2. For BIH catalyst, the loading of hemin on GC was 0.15 mg/cm^2. The inks for JM's 40% Pt/C and JM's Ag-nano were prepared separately with the same procedures. The final coating on the GC electrode was 95% total catalyst and 5% dry Nafion with a Pt loading 0.02 mg/cm^2, and Ag loading 0.10 mg/cm^2. For rotating ring-disk electrode (RRDE) experiment, the GC disk electrode area was 0.247 cm^2, and the Ag or Ag−Co loading was 0.08 mg/cm^2. The ring collection coefficient is 0.37. The catalyst coated electrode was mounted onto a Pine ASR rotator and used as the working electrode. All voltammetrical experiments were performed in argon (Ar) or O$_2$ saturated 0.1 M potassium hydroxide (KOH) solution at room temperature (20 ± 1 °C). A three-electrode glass cell was used for electrochemical study containing three compartments separated by porous ceramic layers. A platinum wire counter electrode and a saturated calomel reference electrode (SCE) were used in the cell. The experimental results are reported based on reversible hydrogen electrode (RHE). The difference between SCE and RHE was experimentally determined with an SCE and a RHE in 0.1 M KOH solution in the same electrochemical cell. The current density reported in this study is based on the geometrical area of the GC disk electrode (mA cm^{-2}), which can be changed to (mA mg^{-1}) by simply multiplying a factor of 10 according to the mass of the catalyst loading.

3. RESULTS AND DISCUSSION

3.1. TEM, STEM, and SAED Results. TEM and STEM is used to explore the materials' morphology and structure in more detail. We first look at the unsupported Ag−Co material. Figure 2 shows STEM-HAADF, TEM and SAED images of
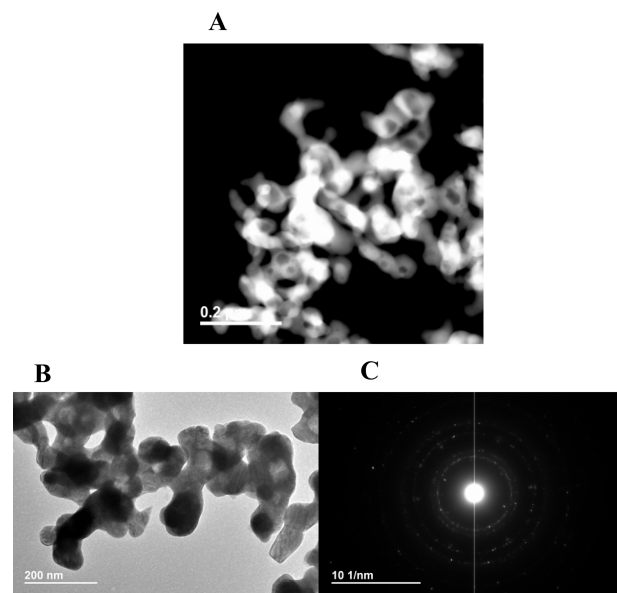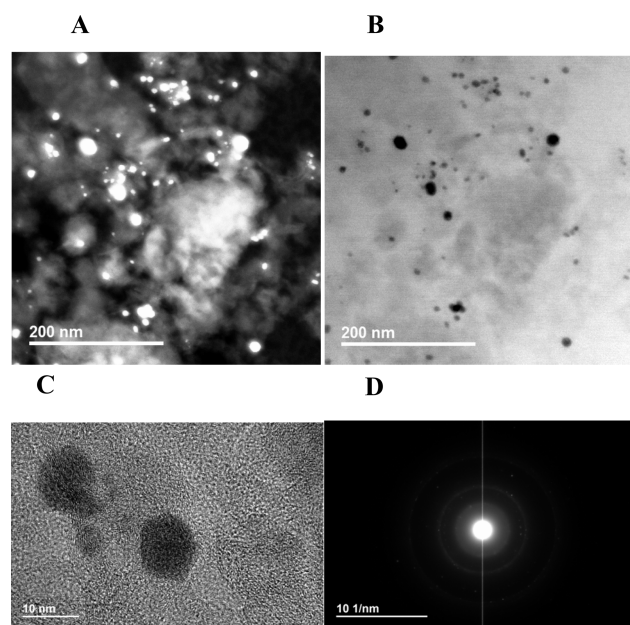

Figure 2. (A) STEM, (B) TEM images, and (C) SAED pattern of unsupported Ag−Co alloy (Co/Ag = 0.10).

unsupported Ag−Co material. Interestingly, the unsupported Ag−Co looks like a dendrite material, where the particles first join together to form short wires, and then, the short wires form dendrimers. The SAED pattern shows that the dendrimers have good crystal structure, which is judged from the multiple clear rings and the bright dots on the rings in the dark field. The TEM images of heat-treated hemin supported on GNP are shown in the Supporting Information (Figure S1). As thin-layers of hemin were deposited on the surfaces of graphene, the material kept graphene's main morphology and structure after heat-treatment. Some darker areas on the graphene sheets are probably because of the deposition of heat-treated hemin.

Figure 3 shows STEM and TEM images and SAED pattern of BIH catalyst. Interestingly, the dendrites seen in the unsupported Ag−Co (Figure 2) disappear and are replaced with smaller particles, with particles size ranging from 5 to 27 nm. It is probably relevant to the use of high surface area GNP support in the synthetic process and ultrasonically processing in preparation of the hybrid catalyst. Figure 3A,B shows images of STEM-HAADF and bright field image (STEM-BF) obtained simultaneously. The STEM-HAADF is highly sensitive to atomic scale, chemical composition and chemical structure, where different elements, compositions, and structures can be recognized. The white dots in the HAADF and black dots in the BF are identified as Ag−Co particles. The cloudy shadows surrounding the dots are relevant to the GNP and carbon materials. The particles of Ag−Co are imbedded in the GNP support with wide particle size distribution. Figure 3C shows a TEM image of the hybrid catalyst, where the particles size is as small as 5 nm. The SAED pattern (Figure 3D) shows some features of amorphous structure, where less rings and bright dots can be seen in the dark field.

Figure 3. (A) STEM-HAADF, (B) STEM-BF, (C) TEM images, and (D) SAED pattern of BIH catalyst (Co/Ag = 0.10) prepared with ultrasonic treatment.

3.2. SEM Results. The SEM images of various catalyst materials are enclosed in Supporting Information (Figure S2). The particle size of Ag−Co is significantly reduced in comparison of pure Ag without alloying, although they are synthesized in the same experimental conditions. The graphene supported Ag−Co/GNP shows that the Ag−Co nanoparticles are dispersed on the large surface of GNP. For BIH catalyst, the Ag−Co nanoparticles are embedded in the mixture of GNP and HT-Hem/GNP.

3.3. XRD Results. Further composition and structure evaluation of the catalysts are completed with XRD. An experiment was designed to prove formation of Ag−Co alloy, instead of a mixture. The method is described as follows. The sample of Ag−Co alloy was heat-treated in air atmosphere at 300 °C, in which the Ag−Co alloy was converted to Ag and Co_3O_4 mixture. Therefore, we obtained the XRD data of Ag and Co_3O_4 mixture. The mixture of Ag and Co_3O_4 was further heat-treated in H_2 atmosphere at 500 °C, in which the Co_3O_4 was converted to pure Co. Thus, we obtained the XRD data of Ag and Co mixture. Figure S3 in the Supporting Information shows XRD patterns of the Ag−Co alloy, mixture of Ag and Co_3O_4, and mixture of Ag and Co, where new peaks appear on the XRD patterns of the two mixtures. The new peaks are identified as Co_3O_4 and Co metals, respectively. Interestingly, the two mixtures originated from the same source of an Ag−Co alloy. The two mixtures have different XRD patterns with that of the Ag−Co alloy. Figure S4 in the Supporting Information shows XRD patterns of Ag−Co alloys with different Co/Ag atomic ratio. Five typical peaks can be seen on the pure Ag XRD pattern. When Ag is alloyed with Co, the position of its peaks has only a slight movement; but all of the peaks become wider. The parameters of the highest peak with Miller index of plane (111) are summarized in Table 1. With an increase in the content of Co in the alloy, the full width at half-maximum (fwhm) of the peaks increases (it is a sign of decrease in crystallite size), and the peak position moves toward the 2θ increasing direction. Simultaneously, the perpendicular distance

Table 1. XRD Data of Ag−Co Catalyst Obtained from the Main Peak at Plane (111) with Different Co/Ag Atomic Ratios

Co/Ag ratio	2θ (deg)	d-spacing (Å)	fwhm (deg)
pure Ag	38.120	2.3588	0.260
0.05	38.121	2.3588	0.339
0.10	38.201	2.3540	0.366
0.20	38.219	2.3529	0.380

between adjacent lattice planes (d-spacing) decreases, which implies that the Ag lattice structure shrinks after alloying with Co.

Figure 4 shows comparison of XRD patterns of BIH catalyst with other catalysts. The peak intensity of the hybrid catalyst
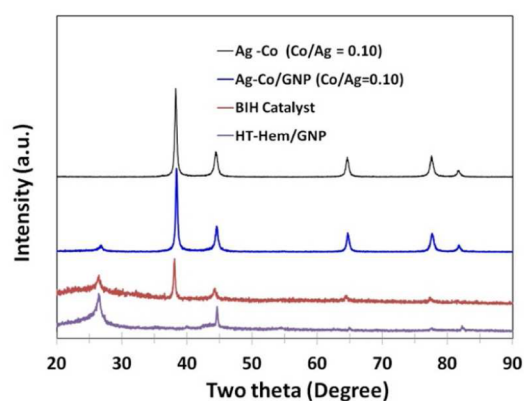
Figure 4. XRD patterns of Ag−Co alloy, Ag−Co/GNP, HT-Hem/GNP, and BIH catalyst coated thin-film.

are apparently reduced due to less content of Ag (14.2% Ag) in the hybrid mixture. A new small peak appears at ∼26.4° (2 theta), which is identified as graphene's specific peak. The parameters of the highest peak at plane (111) are summarized in Table 2. Comparison of Ag−Co/GNP with Ag−Co, the

Table 2. XRD Data Obtained from the Main Peak at Plane (111) for Different Catalyst Materials

materials	2θ (deg)	d-spacing (Å)	fwhm (deg)
pure Ag	38.120	2.3588	0.260
Ag−Co[a]	38.201	2.3540	0.366
Ag−Co/GNP[a]	38.342	2.3457	0.342
BIH catalyst[a]	38.059	2.3625	0.308

[a]Co/Ag ratio = 0.10.

addition of graphene further moves the peak position to larger 2θ value, and decreases the d-spacing, causing Ag lattice structure shrinks. However, for BIH catalyst, the peak position at plane (111) moves back to small 2θ value, and d-spacing becomes the largest, which indicates an expansion of the Ag lattice structure. The shrinkage and expansion in the Ag lattice structure are relevant to Co doping and hemin incorporation, which may change the catalytic property of the catalysts.

3.4. Effect of Co Content in Ag−Co for ORR. The optimal content of Co in the Ag−Co alloy was determined by varying the ratio of Co/Ag in chemical synthesis, and followed by electrochemical analysis. Figure S5 in Supporting Information shows electrochemical behaviors of Ag−Co coated electrodes and their catalytic activity for oxygen reduction. In

argon saturated solution (Figure S5A), oxygen was removed from the electrolyte; and the cyclic voltammograms show typical Ag's surface waves. With increasing the Co content, the higher peaks with larger active electrochemical areas are seen. The catalytic activity was measured with a rotating disk electrode in O_2 saturated electrolyte solution (Figure S5B). The highest catalytic activity was obtained for Co/Ag ratio as 0.10, and its polarization curve has the most positive half wave potential (0.75 V vs RHE). The kinetic parameters for catalytic oxygen reduction can be described with a Tafel equation:

$$E = E^0 + \frac{2.303RT}{\alpha n_\alpha F}\log(i^0) - \frac{2.303RT}{\alpha n_\alpha F}\log(i) \tag{1}$$

$$i^0 = nFK_eC_o \tag{2}$$

Here, E and E^0 are experimental disk potential and thermodynamic electrode potential, respectively, under the experimental conditions (E^0 = 1.23 V vs RHE); α is the electron transfer coefficient in the rate-determining step for oxygen reduction; n_α is the electron transfer number at the rate-determining step; i^0 is the exchange current density, or the current density at the absence of net electrochemical reactions and at zero over potential; i is the disk current; K_e is the electron transfer rate constant in rate-determining step; C_O is oxygen concentration at the electrode surface; n is the electron number of overall oxygen reduction; and, the R, T, and F have their common meanings of universal gas constant (8.314 J·mol^{-1}·K^{-1}), absolute temperature (K), and Faraday's constant (96,485 C·mol^{-1}), respectively.

Figure S5C in the Supporting Information shows Tafel plots obtained from the polarization curves. The linear range of the Tafel plots belongs to low polarization region. For Co/Ag ratio as 0.10, the lowest Tafel slope is obtained, signaling that it has the largest electron transfer coefficient in the rate-determining step for oxygen reduction.

3.5. BIH Catalyst for ORR. First, we synthesized the Ag–Co catalyst without adding hemin, and obtained the similar results as that reported by Lima et al.[30] The Ag–Co catalyzes oxygen reduction by mix-pathways or 2-electron reaction to generate hydrogen peroxide and by 4-electron reaction to generate water, as shown below:

$$O_{2(ad)} + 2H_2O + 4e^- \rightarrow 4OH^- \tag{3}$$

$$O_{2(ad)} + H_2O + 2e^- \leftrightarrow HO_2^- + OH^- \tag{4}$$
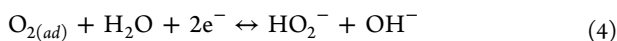
To remove hydrogen peroxide in the products, we added hemin into the Ag–Co catalyst. The mechanism of hemin to remove hydrogen peroxide is described as below:

$$2Fe(II)N_4P + HO_2^- + H_2O \rightarrow 3OH^- + 2Fe(III)N_4P \tag{5}$$

$$2Fe(III)N_4P + 2e^- \rightarrow 2Fe(II)N_4P \tag{6}$$
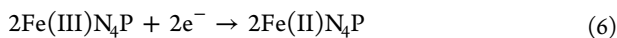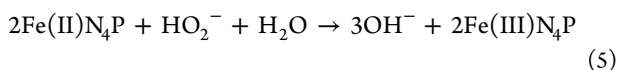
Here, Fe(II)-N4P or Fe(III)-N4P expresses the inner porphyrin ring, which is the functional group to provide catalytic active sites. Using iron porphyrins to remove hydrogen peroxide has been reported in literature.[7,34−36] We have also added graphene nanoplatelets as a catalyst support, which is used to obtain the best dispersion for both the Ag–Co and the hemin catalytic sites. There are numerous reports of adding graphene as catalyst support to improve catalytic performance.[24]

After determining the best Co/Ag ratio in Ag−Co alloy, we synthesized the BIH catalyst with graphene supported hemin and graphene supported Ag−Co by heat-treatment and ultrasonically processing, respectively. After ultrasonic processing, a new composite material is created, which contains new bioinorganic nanointerfaces composed of the Fe−N$_4$P and the Ag−Co catalytic sites supported on GNP. The nanosized bioinorganic interfaces are considerably different from that of inorganic catalytic sites Ag−Co, either in composition or in catalytic mechanisms. The activity of the BIH catalyst is significantly improved. Figure 5 shows polarization curves of
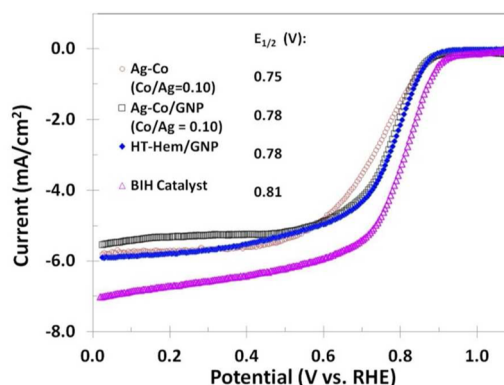
Figure 5. Polarization curves of different catalyst coated electrode in O_2 saturated 0.1 M KOH. Scan rate: 10 mV/s. Rotation rate: 1600 rpm.

different catalyst-coated electrodes for catalytic oxygen reduction. The BIH catalyst has the highest limiting current and the most positive half wave potential in comparison of Ag−Co, Ag−Co/GNP, and HT-Hem/GNP. The Tafel plots of the polarization curves shows that the HT-Hem/GNP has the lowest Tafel slope (59.6 mV/dec), which implies an advantage of fast electron transfer between the catalyst and the oxygen molecules. However, the disadvantage of HT-Hem/GNP is its low concentration of catalytic sites in the material, because each of hemin's large molecules only provides one catalytic site. On the contrary, although the Ag−Co has higher Tafel slope (88.3 mV/dec), it is able to provide high concentration of catalytic sites (each of single Ag atoms at the surface provides one catalytic site). Therefore, a synergic effect can be expected if incorporating the Ag−Co/GNP into HT-Hem/GNP to make a new hybrid material. The new hybrid catalyst material will have both features of high concentration of catalytic sites and fast electron transfer for a high performing catalyst. The concentration of catalytic sites on electrode is relevant to particle loading for an individual experiment. Therefore, we have examined the effect of particle loading on the catalytic performance for oxygen reduction. Figure S6 shows polarization curves of BIH catalyst coated electrode for catalytic oxygen reduction in O2 saturated 0.1 M KOH with different catalyst particle loadings. The best catalytic performance is achieved for 0.1 mg Ag/cm^2 loading. Lower than 0.1 mg Ag/cm^2 of particle loading leads to a decreasing in the catalytic limiting current and a slightly negative shift of half wave potential. Higher than 0.1 mg Ag/cm^2 of particle loading causes inclined limiting current.

3.6. Comparison with Baseline Catalysts. The performance of the hybrid catalyst is further evaluated by comparison with two baseline catalysts. Figure 6A shows polarization curves
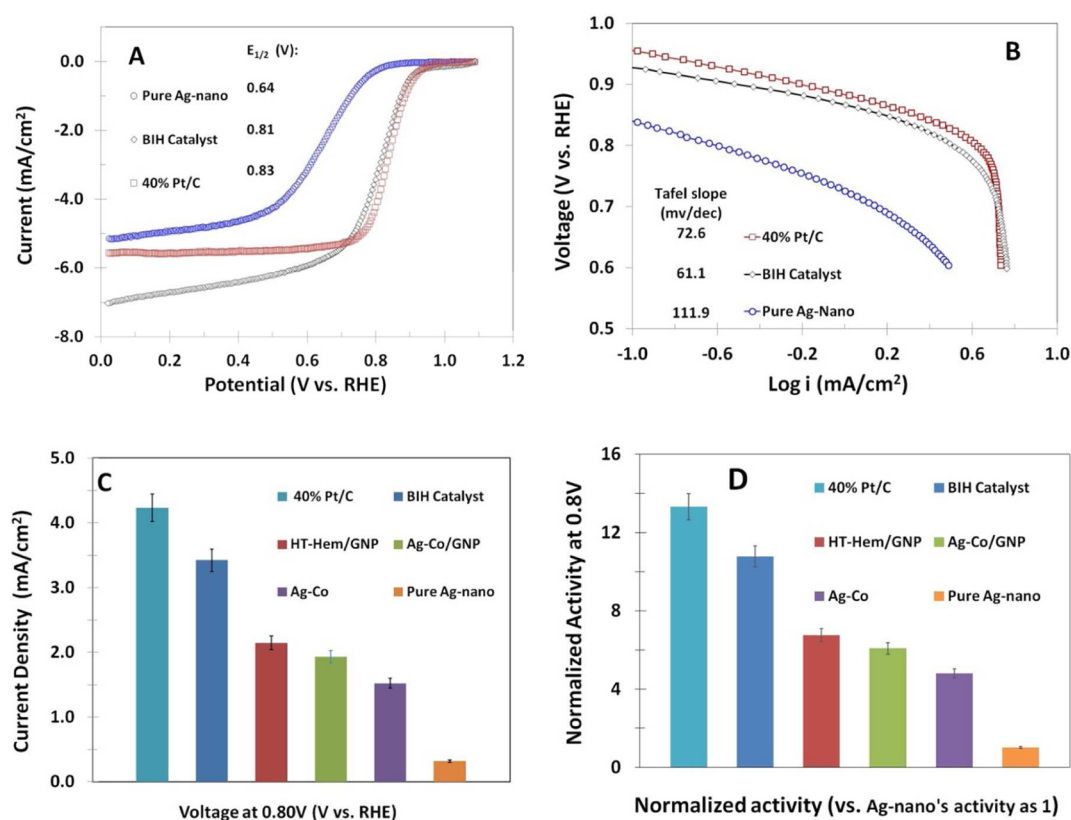
Figure 6. (A) Polarization curves of BIH catalyst and two baseline catalysts coated electrodes in O_2 saturated 0.1 M KOH; (B) Tafel plots of the data from A; (C) Plots of current density at 0.8 V of different catalysts coated electrodes; and (D) Plots of normalized activity based on pure Ag-nano catalyst as 1. Scan rate: 10 mV/s. Rotation rate: 1600 rpm.
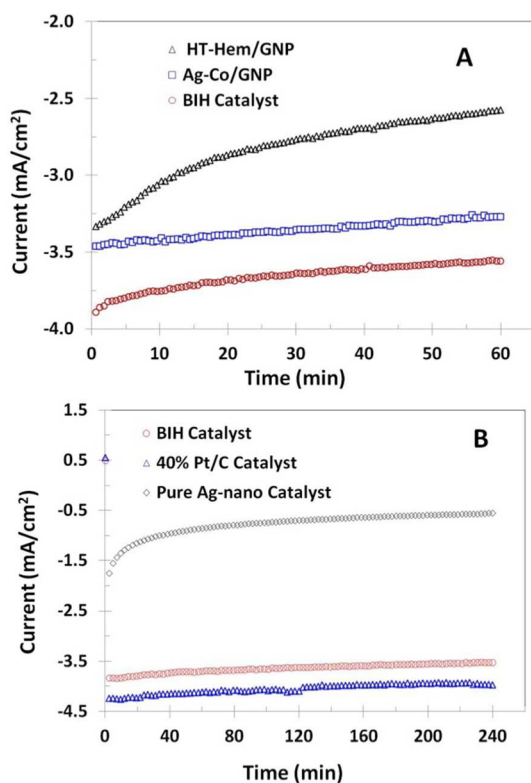
of BIH catalyst and two baseline catalysts coated electrodes for catalytic oxygen reduction. In comparison of pure Ag-nano catalyst (20−40 nm), the hybrid catalyst has 170 mV increase in half wave potential, and 40% increase in limiting current. In comparison of the state-of-the-art catalyst (40% Pt on 60% carbon black), the hybrid catalyst has only 20 mV lower in half wave potential, but it has a higher limiting current in the high polarization region due to a faster kinetic rate. Figure 6B shows Tafel plots of the polarization curves. The hybrid catalyst has even lower Tafel slope than that of the 40%Pt/C catalyst. The large electron transfer coefficient in the rate-determining step for oxygen reduction is expected for the hybrid catalyst. The quantitative comparison of catalytic activity for a series of catalysts is shown in Figures 6C,D. Here, we control the polarization potential at 0.8 V (vs RHE), and compare the current density for catalytic oxygen reduction. There is a 10-fold increase in catalytic activity by comparing the current density of the hybrid catalyst at 0.8 V with that of the pure Ag-nano catalyst (20−40 nm in particle size). Holewinski et al.[31] reported a 5-fold increase in activity for Ag−Co nano catalyst supported on active carbon in comparison of pure Ag nanoparticles for catalytic oxygen reduction in 0.1 M NaOH electrolyte solution. Furthermore, in comparison of 40% Pt/C catalyst, the hybrid catalyst has reached 80% activity of the baseline catalyst at 0.8 V (vs RHE).

The Co particles at the surface of the Ag−Co alloy are unstable, and become $Co(OH)_2$ in alkaline solution. However, the Co particles within the inner side of the Ag−Co crystal are relative stable, which may be gradually lost into the electrolyte and leaving fresh nanostructures at the Ag−Co particles, casing

more active surface area. The stability of the BIH catalyst is evaluated with chronoamperometric voltammetry. Figure 7 shows chronoamperometric curves of different catalyst coated electrodes, where the potential is held at 0.7 V (vs RHE), and recording the current variation with time (current−time curve). As shown in Figure 7A, the current−time curve of the BIH catalyst has higher current density than that of either HT-Hem/GNP or Ag−Co/GNP, and smaller slope of current decreasing with time. The hybrid catalyst is further compared with two baseline catalysts, pure Ag-nano (20−40 nm) and 40% Pt/C. Figure 7B shows the 240 min chronoamperometric experiment at the catalyst coated rotating disk electrodes, where the rotation rate was 900 rpm and O_2 was continuously passing into 0.1 M KOH solution. The hybrid catalyst has much higher current density than that of the Ag-nano catalyst. In comparison to the 40% Pt/C catalyst, the hybrid catalyst has only slightly lower current density but the same stability.

The resistance to methanol of heat-treated transition metal (Fe, Co, Cu, V, Ni) porphyrins has been reported and discussed in detail in our previous publication.[7] The heat-treated hemin belongs to the same type of macrocyclic compound as that of Fe porphyrins. It is clear that the heat-treated hemin is highly tolerant to methanol. The Ag nano catalyst is also highly tolerant to methanol, which has been reported in our previous publication.[37] Since the active sites of the BIH catalyst are from Ag atoms and heat-treated hemin, apparently, the BIH catalyst is also tolerant to methanol. In the present work, we have no attempt to further study the tolerance of BIH catalyst to methanol.

Figure 7. Chronoamperometric curves of different catalyst-coated electrodes at 0.7 V (vs RHE) and 900 rpm in O_2 saturated 0.1 M KOH. (A) Comparison of BIH catalyst, HT-Hem/GNP, and Ag−Co/GNP. (B) Comparison of BIH catalyst and two baseline catalysts; here, 40% Pt/C loading is 0.10 mg/cm^2, Pt loading is 0.04 mg/cm^2, and Ag loading is 0.1 mg/cm^2.

3.7. Oxygen Reduction Kinetic and Mechanisms.

Further exploration of the kinetics and mechanisms for catalytic oxygen reduction is completed by rotating disk electrode (RDE) and rotating ring-disk electrode (RRDE) experiments. Figure 8A shows polarization curves of BIH catalyst coated electrode at different rotation rates. The kinetic process can be described with the Koutecky−Levich equation:

$$i_L = 0.620 n F A D_O^{2/3} \omega^{1/2} \nu^{-1/6} C_o^* \tag{7}$$

$$i_k = n F A K_f(E) C_o^* \tag{8}$$

$$i^{-1} = i_k^{-1} + i_L^{-1} \tag{9}$$

$$i^{-1} = \frac{1}{i_k} + \frac{1}{0.620 n F A D_O^{2/3} \nu^{-1/6} C_o^* \omega^{1/2}} \tag{10}$$

Here, i_L is the Levich current for species O's electrode reaction by diffusion controlled process; A (cm^2) is the electrode area; D_O ($cm^2 \cdot s^{-1}$) is diffusion coefficient of species O; ω (s^{-1}) is rotation rate (= $2\pi f = 2\pi \times rpm/60$); ν ($cm^2 \cdot s^{-1}$) is viscosity of electrolyte solution; C_O^* is oxygen concentration in bulk electrolyte solution (in O_2 saturated electrolyte, $C_O^* = 1.3 \times 10^{-6}$ mol·cm^{-3});[38] i_k is kinetic current of O species at the electrode surface; and K_f (E) ($cm \cdot s^{-1}$) is rate constant of oxygen reduction at potential E.

Figure 8B shows Koutecky−Levich plots of i^{-1} versus $\omega^{-1/2}$. The Koutecky−Levich plots obtained at different potentials from the experiments are straight lines, and are parallel to the calculated curve for 4-electron oxygen reduction by diffusion
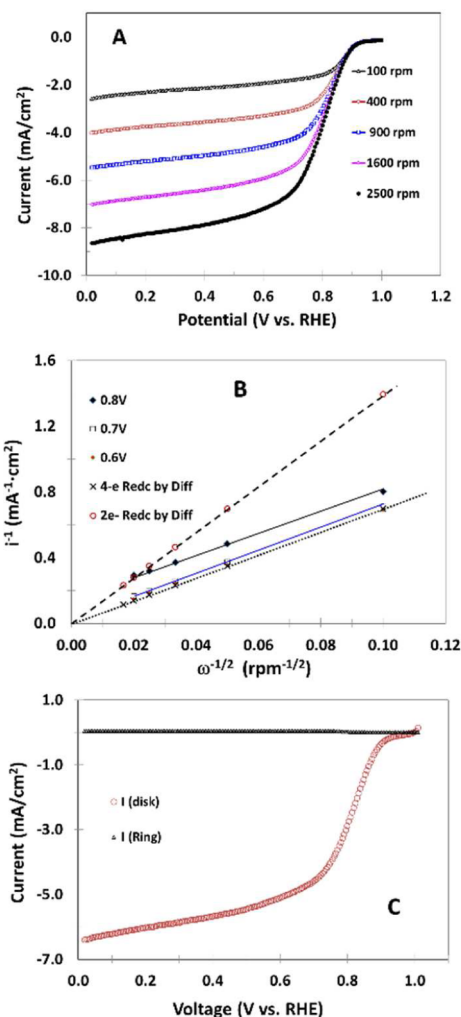
Figure 8. (A) Polarization curves of BIH catalyst coated electrode at different rotation rates in O2 saturated 0.1 M KOH. Scan rate: 10 mv/s. (B) Koutecky−Levich plots of the data in A. (C) Voltammogram of BIH catalyst-coated disk and Pt-ring electrode in O_2-saturated 0.1 M KOH. Scan rate: 10 mv/s. Rotation rate: 1600 rpm.

controlled process. It indicates that the catalytic process belongs to 4-electron oxygen reduction to produce water. The rate constants for oxygen reduction at different potentials are 1.2×10^{-2} cm·s^{-1} (0.8 V), 6.8×10^{-2} cm·s^{-1} (0.7 V), and 12.5×10^{-2} cm·s^{-1} (0.6 V), respectively. The rate constant (at 0.6 V) is 4 times higher than of that of Ag/GNP (3.2×10^{-2} cm·s^{-1} at 0.6 V) reported by Jiang et al.[37] Further proof of 4-electron reduction of oxygen at the hybrid catalyst is provided with RRDE experiments. Figure 8C shows polarization curves of the hybrid catalyst coated GC rotating disk and Pt-ring electrode. The ring electrode was held at 1.4 V (vs RHE) to fully oxidize the intermediate product, hydrogen peroxide, which is collected from the disk electrode in the electrochemical process. As expected, the ring-current is too small to be counted. As demonstrated by the RRDE experiment, the catalytic process at the hybrid catalyst belongs to 4-electron oxygen reduction to produce water.

Heat-treated macrocyclic organic compounds, such as porphyrins and phthalocyanines, have demonstrated very promising performance as non-noble metal catalysts for oxygen reduction. However, the chemical structure of heat-treated macrocyclic organic compounds has been a major concern

since the 1980s. In recent years, more researchers have used X-ray absorption fine structure spectroscopy (XAFS) to explore the remaining product after heat-treated macrocycles, and the chemical structures are clearer. Choi et al.[39] studied the iron phthalocyanine (FePc) supported on high surface area carbon by XAFS. They suggested that (FePc)2O was converted to FePc in the range of 500−600 °C, and the Fe−N$_4$P structure is essential for maintaining the catalytic activity. Schulenburg et al.[40] investigated the structure and the stability of heat-treated iron(III) tetramethoxy-phenylporphyrin chloride. They concluded that nitrogen atom is bonded at the edge of graphene layers as pyrrole and pyridine-type nitrogen. Zhang et al.[41] studied heat-treated iron polyphthalocyanine with XAFS. Their results showed that the Fe−N$_4$P structure was produced by the high-temperature treatment. According to Schulenburg's results[40] by Fe−Mössbauer spectrum of the FeTMPP, the Fe atom remains after heat-treatment.

We have completed elemental analysis of the hemin supported on the GNP. The results of elemental analysis for HT-hemin/GNP heat-treated at 600 °C in N2 atm is listed in Table S1. Our elemental results is consisted with the report by Schulenburg el at.[40] We have also completed thermogravimetric (TGA) analysis and elemental analysis to further understand the chemical structures of the heat-treated hemin. We analyzed the data of the TGA curve and calculated the weight loss by gradually removing the atoms in the hemin molecule. Figure S7 in the Supporting Information shows hemin's mass change with temperature by TGA analysis. The hemin molecule first loses one Cl atom at temperatures lower than 320 °C; two −COO groups at 320−430 °C, and 30 H atoms and 6 C atoms of the outer branches at 430−540 °C. Then, it becomes relatively stable at 540−710 °C before losing another 6 C atoms linked to the Fe−N$_4$P ring in the hemin molecule. Above 850 °C, more carbon atoms are losr, and the FeN$_4$ ring decomposes. The analysis of TGA results is consistent with the results reported in literature.[39−41] Although the hemin molecule loses its outer groups after heat-treatment at 600 °C, its inner functional group Fe−N$_4$P still exists, which grants the catalytic activity.

According to the kinetic study with RDE and RRDE methods, we proposed a catalytic model to explain ORR at the BIH catalyst, which is made of HT-hemin, Ag−Co alloy and GNP, as shown in Figure 9. Here, the Ag atoms (blue spheres) provide inorganic catalytic sites; and the Co atoms (golden spheres) are the atoms of the guest element in the Ag−Co alloy to enhance the activity of Ag. The heat-treated hemin provides the biocatalytic sites. After heat-treatment in nitrogen atmosphere, the hemin molecules lost hydrogen and oxygen atoms, but the inner structures of the hemin molecules remained.[4,5,39−41] Four nitrogen atoms (green spheres) and one iron atom (gray sphere) remained in each of the hemin molecules after heat-treatment. The GNP is the catalytic support used for uniform dispersion of the catalytic sites. Each of the Fe−N$_4$P structures is surrounded by the nearby Ag-catalytic sites. As long as Ag-sites at the surface of the Ag−Co nano particles approach to a Fe−N$_4$P site in certain short distance, an Ag−Fe bridge catalytic structure formed. The oxygen molecules may be catalytically reduced by the Ag−Fe-bridge structure to produce water through 4-electron reduction,[2,3,42] which involves a breakage of the O−O bond.

4. CONCLUSION

In this study, we have demonstrated a method of making nanostructured BIH catalyst that contains three main steps: (1) heat-treatment of bio material, hemin, supported on GNP, (2) synthesis of nanostructured Ag−Co alloy supported on GNP; and (3) ultrasonic processing of the two materials obtained from steps 1 and 2 to create new nanostructured bioinorganic interfaces between the Fe−N$_4$P and Ag−Co catalytic sites. The overall synthesis is simple, and it is easy to scale up for manufacturing production. The BIH catalyst was fully characterized with TEM, STEM, SEM, XRD, TGA, elemental analysis, and electrochemical methods.

The BIH catalyst belongs to a composite material, which takes the advantages of the combined features of the bio and inorganic materials. A 10-fold improvement in catalytic activity is achieved in comparison of pure Ag nanoparticles (20−40 nm). The BIH catalyst reaches 80% activity of the baseline catalyst (40% Pt and 60% active carbon). Comparable catalytic stability for the BIH catalyst and the Pt catalyst is observed by chronoamperometric experiment. The BIH catalyst catalyzes 4-electron oxygen reduction to produce water with fast kinetic rate. The rate constant obtained from the BIH catalyst (at 0.6 V vs RHE) is 4 times higher than that of pure Ag nanocatalyst supported on graphene nano platelets (Ag/GNP). A catalytic model is proposed to explain ORR at the BIH catalyst. In a short summary, the BIH catalyst has the features of low cost, high performance, and easy synthesis, which fit the basic requirements of practical applications for high performing alkaline fuel cells.

■ ASSOCIATED CONTENT

Ⓢ Supporting Information

The Supporting Information is available free of charge on the ACS Publications website at DOI: 10.1021/acsami.5b04714.

> TEM, XRD, SEM, TGA, elemental analysis, and electrochemical data of ORR. (PDF)

■ AUTHOR INFORMATION
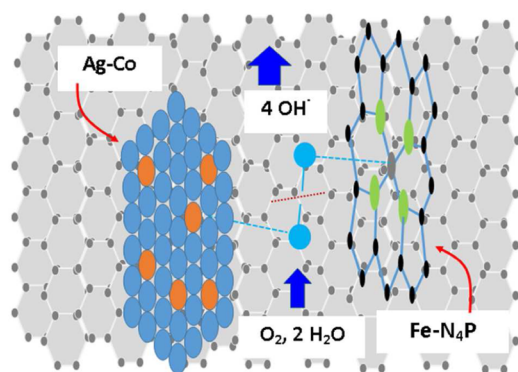
Corresponding Author

* Phone: 301-394-0295. E-mail: Rongzhong.jiang.civ@mail.mil.

Author Contributions

The manuscript was written through contributions of all authors. All authors have given approval to the final version of the manuscript.

Notes

The authors declare no competing financial interest.

Figure 9. Catalytic model of oxygen reduction reaction at the BIH catalyst, which contains bioinorganic nanointerfaces between Fe−N$_4$P and Ag−Co supported on GNP.

■ ABBREVIATIONS

ORR   oxygen reduction reaction
GNP   graphene nanoplatelets
TEM   transmission electron microscope
STEM   scanning transmission electron microscope
HAADF   high angle annular dark field
SAED   selected area electron diffraction
EDS   energy-dispersive X-ray spectroscopy
XRD   X-ray diffraction
TGA   thermogravimetric analysis
RHE   reversible hydrogen electrode

■ REFERENCES

(1) Marcinkoski, J.; James, B. D.; Kalinoski, J. A.; Podolski, W.; Benjamin, T.; Kopasz, J. Manufacturing Process Assumptions Used in Fuel Cell System Cost Analyses. *J. Power Sources* **2011**, *196*, 5282−5292.

(2) Collman, J. P.; Marrocco, M.; Denisevich, P.; Koval, C.; Anson, F. C. Potent Catalysis of The Electroreduction of Oxygen to Water by Dicobalt Porphyrin Dimers Adsorbed on Graphite Electrodes. *J. Electroanal. Chem. Interfacial Electrochem.* **1979**, *101* (1), 117−122.

(3) Collman, J. P.; Denisevich, P.; Konai, Y.; Marrocco, M.; Koval, C.; Anson, F. C. Electrode Catalysis of The Four-Electron Reduction of Oxygen to Water by Dicobalt Face-to-Face Porphyrins. *J. Am. Chem. Soc.* **1980**, *102* (19), 6027−6036.

(4) van Veen, J. A. R.; Colijn, H. A.; van Baar, J. F. On The Effect of A Heat Treatment on The Structure of Carbon-Supported Metalloporphyrins And Phthalocyanines. *Electrochim. Acta* **1988**, *33* (6), 801−804.

(5) Dong, S. J.; Jiang, R. Z. Research on Chemically Modified Electrodes. Electrocatalytic Reduction of Dioxygen by Iron Tetraphenylporphyrin Modified Glassy Carbon Electrode with Heat Treatment. *Ber. Bunsenges. Phys. Chem.* **1987**, *91* (4), 479−484.

(6) Gojkovic, S. L.; Gupta, S.; Savinell, R. F. Heat-treated Iron (III) Tetramethoxy-Phenyl Porphyrin Chloride Supported on High-Area Carbon As An Electrocatalyst for Oxygen Reduction: Part II. Kinetics of Oxygen Reduction. *J. Electroanal. Chem.* **1999**, *462* (1), 63−72.

(7) Jiang, R. Z.; Chu, D. Remarkably Active Catalysts for The Electroreduction of O2 to H2O for Use in An Acidic Electrolyte Containing Concentrated Methanol. *J. Electrochem. Soc.* **2000**, *147* (12), 4605−4609.

(8) Wang, Y. J.; Wilkinson, D. P.; Neburchilov, V.; Song, C. J.; Guest, A.; Zhang, J. J. Ta And Nb Co-Doped TiO2 And Its Carbon-Hybrid Materials for Supporting Pt−Pd Alloy Electrocatalysts For PEM Fuel Cell Oxygen Reduction Reaction. *J. Mater. Chem. A* **2014**, *2*, 12681−12685.

(9) Zhu, W.; Zeng, C. C.; Zheng, J. P.; Liang, R.; Zhang, C.; Wang, B. Preparation of Buckypaper Supported Pt Catalyst for PEMFC Using A Supercritical Fluid Method. *Electrochem. Solid-State Lett.* **2011**, *14*, B81−83.

(10) Ebbesen, T. W.; Ajayan, P. M. Large-Scale Synthesis of Carbon Nanotubes. *Nature* **1992**, *358*, 220−222.

(11) Che, G. L.; Lakshmi, B. B.; Fisher, E. R.; Martin, C. R. Carbon Nanotube Membrane for Electrochemical Energy Storage And Production. *Nature* **1998**, *393*, 346−349.

(12) McClure, J. P.; Jiang, R. Z.; Chu, D.; Fedkiw, P. S. Oxygen Electroreduction on Fe- or Co-Containing Carbon Fibers. *Carbon* **2014**, *79*, 457−469.

(13) Liu, P.; Kong, J. R.; Liu, Y.; Liu, Q.; Zhu, H. Graphitic Mesoporous Carbon Based on Aromatic Polycondensation as Catalyst Support for Oxygen Reduction Reaction. *J. Power Sources* **2015**, *278*, 522−526.

(14) Zhou, X. J.; Qiao, J. L.; Yang, L.; Zhang, J. J. A Review of Graphene-based Nanostructural Materials for Both Catalyst Supports and Metal-Free Catalysts in PEM Fuel Cell Oxygen Reduction Reactions. *Adv. Energy Mater.* **2014**, *4*, 1301523.

(15) Rong, C.; Jiang, R. Z.; Sarney, W.; Chu, D. Ultrasound Assisted Micro-emulsion for Synthesis of Pt And PtCo Nano-Particles. *Electrochim. Acta* **2010**, *55*, 6872−6878.

(16) Guo, S. J.; Zhang, S.; Su, D.; Sun, S. H. Seed-mediated Synthesis of Core/Shell FePtM/FePt (M = Pd, Au) Nanowires and Their Electrocatalysis for Oxygen Reduction Reaction. *J. Am. Chem. Soc.* **2013**, *135*, 13879−13884.

(17) Chen, C.; Kang, Y. J.; Huo, Z. Y.; Zhu, Z. W.; Huang, W. Y.; Xin, H. L.; Snyder, J. D.; Li, D. G.; Herron, J. A.; Mavrikakis, M.; Chi, M. F.; More, K. L.; Li, Y. D.; Markovic, N. M.; Gabor, A.; Somorjai, G. A.; Yang, P. D.; Stamen-kovic, V. R. Highly Crystalline Multimetallic Nanoframes with Three-dimensional Electrocatalytic Surfaces. *Science* **2014**, *343*, 1339−1343.

(18) Tsai, Y. H.; Chiu, C. Y.; Huang, M. H. Fabrication of Diverse Cu2O Nanoframes through Face-Selective Etching. *J. Phys. Chem. C* **2013**, *117*, 24611−24617.

(19) McEachran, M.; Keogh, D.; Pietrobon, B.; Cathcart, N.; Gourevich, I.; Coombs, N.; Kitaev, V. Ultrathin Gold Nanoframes through Surfactant-free Templating of Faceted Pentagonal Silver Nanoparticles. *J. Am. Chem. Soc.* **2011**, *133*, 8066−8069.

(20) Chen, H. M.; Liu, R. S.; Lo, M. Y.; Chang, S. H.; Tsai, L. D.; Peng, Y. M.; Lee, J. F. Hollow Platinum Spheres with Nano Channels: Synthesis and Enhanced Catalysis for Oxygen Reduction. *J. Phys. Chem. C* **2008**, *112*, 7522−7526.

(21) Li, R.; Hao, H.; Cai, W. B.; Huang, T.; Yu, A. S. Preparation of Carbon Supported Pd−Pb Hollow Nanospheres And Their Electrocatalytic Activities for Formic Acid Oxidation. *Electrochem. Commun.* **2010**, *12*, 901−904.

(22) Tuaev, X.; Rudi, S.; Petkov, V.; Hoell, A.; Strasser, P. In Situ Study of Atomic Structure Transformations of Pt-Ni Nano-Particle Catalysts during Electrochemical Potential Cycling. *ACS Nano* **2013**, *7*, 5666−5674.

(23) Liang, Z. X.; Song, H. Y.; Liao, S. J. Hemin: A Highly Effective Electrocatalyst Mediating the Oxygen Reduction Reaction. *J. Phys. Chem. C* **2011**, *115*, 2604−2610.

(24) Jiang, R. Z.; Tran, D. T.; McClure, J.; Chu, D. Heat-Treated Hemin Supported On Graphene Nano platelets for The Oxygen Reduction Reaction. *Electrochem. Commun.* **2012**, *19*, 73−76.

(25) Jiang, R. Z.; Tran, D. T.; McClure, J.; Chu, D. Increasing The ElectrochemicaLy Available Active Sites For Heat-treated Hemin Catalysts Supported On Carbon Black. *Electrochim. Acta* **2012**, *75*, 185−190.

(26) Liu, P.; Chen, C. G.; Guo, C. Z.; Du, M.; Wu, H. J.; Yin, W. A Non-noble Metal Electrocatalyst for Oxygen Reduction Reaction Using Egg-white Protein as Nitrogen Source. *Asian J. Chem.* **2014**, *26*, 2523−2526.

(27) Maruyama, J.; Abe, I. Carbonized Hemoglobin Functioning as a Cathode Catalyst for Polymer Electrolyte Fuel Cells. *Chem. Mater.* **2006**, *18*, 1303−1311.

(28) Beer, S. Z.; Sandier, Y. L. Oxygen Reduction at Silver and Silver-based Alloy Electrodes. *J. Electrochem. Soc.* **1965**, *112*, 1133−1136.

(29) Yang, Y. F.; Zhou, Y. H. Particle Size Effects for Oxygen Reduction on Dispersed Silver + Carbon Electrodes in Alkaline Solution. *J. Electroanal. Chem.* **1995**, *397*, 271−278.

(30) Lima, F. H. B.; de Castro, J. F. R.; Tician-elli, E. A. Silver-Cobalt Bimetallic Particles for Oxygen Reduction in Alkaline Media. *J. Power Sources* **2006**, *161*, 806−812.

(31) Holewinski, A.; Idrobo, J. C.; Linic, S. High Performance Ag−Co Alloy Catalysts for Electrochemical Oxygen Reduction. *Nat. Chem.* **2014**, *6*, 828−834.

(32) Guo, J. S.; Li, H. X.; He, H.; Chu, D.; Chen, R. R. CoPc- and CoPcF16-Modified Ag Nanoparticles as Novel Catalysts with Tunable Oxygen Reduction Activity in Alkaline Media. *J. Phys. Chem. C* **2011**, *115*, 8494−8502.

(33) Esmaeili, A.; Entezari, M. H. Facile and Fast Synthesis of Graphene Oxide Nanosheets via Bath Ultrasonic Irradiation. *J. Colloid Interface Sci.* **2014**, *432*, 19−25.

(34) Jiang, R. Z.; Chu, D. Comparative Study of CoFeNx/C Catalyst Obtained by Pyrolysis of Hemin and Cobalt Porphyrin for Catalytic Oxygen Reduction in Alkaline and Acidic Electrolytes. *J. Power Sources* **2014**, *245*, 352−361.

(35) Wu, G.; Nelson, M.; Ma, S.; Meng, H.; Cui, G. F.; Shen, P. K. Synthesis of Nitrogen-Doped Onion-Like Carbon and Its Use in Carbon-Based CoFe Binary Non-Precious-Metal Catalysts For Oxygen Reduction. *Carbon* **2011**, *49*, 3972−3982.

(36) Li, S.; Zhang, L.; Kim, J.; Pan, M.; Shi, Z.; Zhang, J. J. Synthesis of Carbon-Supported Binary FeCoN Non-Noble Metal Electrocatalysts for the Oxygen Reduction Reaction. *Electrochim. Acta* **2010**, *55*, 7346−7353.

(37) Jiang, R. Z.; Moton, E.; McClure, J. P.; Bowers, Z. A. Highly Active and Alcohol-tolerant Cathode Electrocatalyst Containing Ag Nanoparticles Supported on Graphene. *Electrochim. Acta* **2014**, *127*, 146−152.

(38) Jiang, R. Z.; Anson, F. C. The Origin of Inclined Plateau Currents in Steady-state Voltammograms for Electrode Processes Involving Electrocatalysis. *J. Electroanal. Chem. Interfacial Electrochem.* **1991**, *305*, 171−184.

(39) Choi, H. J.; Kwag, G.; Kim, S. Electrochemical and XAFS Investigation of Nitrite Reduction by Heat-Treated μ-Oxo Derivative of Iron Phthalocyanine Supported on High Area Carbon. *J. Electroanal. Chem.* **2001**, *508*, 105−114.

(40) Schulenburg, H.; Stankov, S.; Schunemann, V.; Radnik, J.; Dorbandt, I.; Fiechter, S.; Bogdanoff, P.; Tributsch, H. Catalysts for the Oxygen Reduction from Heat-Treated Iron(III) Tetramethoxyphenylporphyrin Chloride: Structure and Stability of Active Sites. *J. Phys. Chem. B* **2003**, *107*, 9034−9041.

(41) Zhang, R.; Peng, Y. X.; Li, Z. P.; Li, K.; Ma, J.; Liao, Y.; Zheng, L. R.; Zuo, X.; Xia, D. G. Oxygen Electroreduction on Heat-treated Multi-walled Carbon Nanotubes Supported Iron Polyphthalocyanine in Acid Media. *Electrochim. Acta* **2014**, *147*, 343−351.

(42) Yeager, E. B. Electrocatalysts for O2 Reduction. *Electrochim. Acta* **1984**, *29*, 1527−1537.